IUST
Iran University of Science and Technology

Iranian Journal of Electrical and Electronic Engineering

Journal Homepage: ijeee.iust.ac.ir

Advanced Inductor Current Control Schemes of Grid-Connected Quasi-Z-Source Inverter in Wind Turbine-based PMSG

Kazem Mokhtari*, Shokrollah Shokri-Kojori* and Mahdi Aliyari-Shoorehdeli*

Abstract: This paper presents three advanced inductor current control schemes for grid-connected Quasi-Z-Source inverters with LCL filters in wind power applications. The first scheme employs a sliding mode control (SMC)-based controller to regulate inductor current via a shoot-through ratio. The second scheme introduces a fuzzy gain scheduling PID controller (FGS-PID), which replaces the SMC for inductor current regulation. The FGS-PID utilizes fuzzy rule-based reasoning to dynamically adjust PID gains based on the error signal and its derivative, enhancing transient response, reducing oscillations, and ensuring system stability and accuracy. The performance of these controllers is evaluated against a traditional PI controller under identical conditions. Comprehensive simulations on MATLAB/SIMULINK and experimental hardware-in-the-loop (HIL) testing demonstrate that: (i) SMC reduces capacitor voltage ripple to ±5 V (0.35%)—a 62% improvement over the PI controller (±13 V, 0.92%)—and limits grid current total harmonic distortion (THD) to ≤1.8%; (ii) FGS-PID achieves intermediate performance (±10 V ripple, ≤2.5% THD) with only heuristic tuning; and (iii) SMC maintains stable operation with 31.7% current overshoot during grid fault recovery, compared to 41.1% for PI. The results provide valuable insights into the strengths and limitations of each controller, offering a foundation for future advancements in wind power systems.

Keywords: Quasi Z-Source inverter, Wind energy, Fuzzy PID controller, Sliding mode controller, Hardware-in-the-Loop.

1 Introduction

Wind energy conversion systems (WECS) are widely regarded as a promising alternative to fossil fuels. Their advantages include zero carbon emissions, abundant availability, cost-effective operation, and high energy output [1]. In these systems, the turbine captures wind energy and converts it into mechanical torque, which the generator then transforms into electrical power. However, the fluctuating nature of wind speed poses a persistent challenge to both the stability and efficiency of WECS [2]. Wind turbines are broadly categorized into fixed-speed and variable-speed types, with the latter being preferred for their ability to operate effectively across a wider range of wind speeds [3]. Among the various components used in variable-speed wind turbines, the permanent magnet synchronous generator (PMSG) is particularly notable for its advantages, including higher efficiency, improved power factor, elimination of gearbox systems, and reduced maintenance requirements. Additionally, PMSG-based turbines enable flexible control of active and reactive power, making them highly suitable for wind energy applications. Despite these advantages, there remains room for improvement in the

Iranian Journal of Electrical & Electronic Engineering, 2026.
Paper first received 3 10 2025 and accepted 6 9 2026.
* The authors are with the Department of Faculty of Electrical Engineering K. N. Toosi University of Technology, Seyed-Khandan bridge, Shariati Ave. Tehran, 98, Iran.
E-mails: k.mokhtari666@gmail.com, aliyari@kntu.ac.ir.
Corresponding Author: Mahdi Aliyari-Shoorehdeli.

design and control structures of PMSG-based systems, which can be complex and challenging to optimize [4].

Integrating wind energy into the utility grid relies heavily on power electronic converters. Conventional systems typically employ a two-stage topology, consisting of a DC–DC boost converter cascaded with a voltage source inverter (VSI) [5]. However, the quasi-Z-source inverter (qZSI) has emerged as a more efficient alternative, capable of performing both voltage boosting and DC-to-AC conversion in a single stage. This simplifies the system architecture and enhances reliability [6, 7]. The qZSI is particularly advantageous for PMSG-driven wind turbines, as it can effectively handle variable wind speeds and grid disturbances [8]. Its continuous input current feature also makes it ideal for wind turbine applications, enabling maximum power extraction [9]. Furthermore, the qZSI mitigates dynamic issues in grid-connected systems by reducing the damping of grid-connected converters, which is essential for maintaining system stability [10, 11].

The control objectives of the qZSI are diverse, focusing on improving system performance and reliability across different applications. Primary goals include maintaining a stable DC-link voltage and delivering high-quality AC output, which are particularly crucial for wind energy systems and electric vehicle applications [12-14]. Variable Weight Coefficient MPC (V-MPC) and Finite Switching Sequence MPC (FSS-MPC) are applied to reduce current ripple and THD, thereby improving power quality [15]. Other control schemes, such as input current-based sinusoidal pulse width modulation (SPWM) and capacitor voltage, manage DC bus voltage and shoot-through states, enhancing robustness against parameter variations [16]. Combining linear PWM and FCS-MPC ensures high-quality waveforms and fast transient response [17]. Proportional integral and Proportional resonant control strategies are also implemented to achieve simultaneous control of both AC and DC sides, ensuring stable operation in buck and boost modes [18]. Dual-loop lead–proportional controllers ensure robust DC-link regulation and suppress high-frequency oscillations. [19]. In [20], a novel multi-objective control strategy integrates sliding mode control (SMC) to regulate inductor current and maintain constant capacitor voltage, ensuring low current ripple and pure sinusoidal load current with low THD.

Among the various control objectives in the qZSI-based wind energy system, the control of the DC side inductor current is of utmost importance. This is because it has a direct bearing on the ability to transfer energy from the generator to the DC link and thus track the maximum power point under varying wind speeds. In addition to this, the inductor current is closely coupled with the capacitor voltage and the shoot-through duty cycle, making it a nonlinear control problem. Conventional PI controllers may have simple structures but may not perform well in the presence of uncertainties. This calls for the evaluation of advanced control strategies that can address nonlinearities in the control problem to improve robustness. This work proposes the design of a SMC and a FGS-PID controller, both of which have significant theoretical advantages for the control problem.

A principal goal in wind energy conversion is to create a system that is efficient, robust, and reliable. The qZSI helps achieve this by consolidating the entire DC-AC conversion process—including buck and boost functions—into a single stage. This consolidation reduces architectural complexity and improves overall efficiency [9]. It also facilitates maximum power point tracking (MPPT) to optimize wind energy capture, often using algorithms like hill-climbing or fuzzy logic-based optimization [21, 22]. Additionally, the control system must manage active and reactive power to maintain grid stability and comply with grid codes, often employing techniques like Space Vector Modulation adapted for Z-source converters [23]. In stand-alone systems, advanced control measures, such as Proportional-Resonant (PR) regulators and model predictive control (MPC) with optimized switching vectors, are implemented to enhance dynamic performance and reduce thermal stress on power devices [24]. Despite their advantages, conventional MPC methods have several well-known limitations. They typically impose a heavy computational load, suffer from inconsistent switching frequencies, and require a complex, manual process for tuning weighting parameters.

This paper puts forward the following contributions:

- In order to address the coupled dynamics of DC-side inductor current and capacitor voltage, which is one of the major issues in the control of qZSI, this paper presents a cascaded control strategy comprising three levels of control: an outer voltage control loop with a bandwidth of 5.31 rad/s, a middle grid current control loop with 226 rad/s bandwidth, and an inner inductor current control loop with 19.34 rad/s bandwidth. The proposed control strategy facilitates the MPPT operation under wind speed fluctuations from 6 to 12 m/s. The structure uses a main dual-loop to manage DC-side capacitor voltages and active AC, supplemented by two specialized feedback loops that regulate the DC-side inductor and reactive currents.
- Next, we developed a Sliding Mode Controller that regulates inductor current by actively managing the converter's shoot-through state. The core of this controller is its switching surface, which we define as a function of both the DC-side inductor current and the capacitor voltage.
- A fuzzy gain scheduling scheme is proposed for the PID controller to regulate inductor current, replacing

SMC. A comparative analysis of the two control strategies with a conventional PI controller is conducted under identical operational settings, evaluating their performance under fluctuating wind speeds.

- Experimental hardware-in-the-loop (HIL) validation verifies that the proposed sliding mode controller (SMC) effectively minimizes the capacitor voltage ripple to ±5 V (0.35%) and the grid current total harmonic distortion (THD) to ≤1.8%, which is a 40% reduction compared to the performance of the traditional PI controller under the same wind speed and grid disturbance conditions. We confirmed this HIL tests that pushed the system against a series of difficult scenarios: fluctuating wind speeds, shifting reactive power demands, and even grid disturbances like voltage sags.

This paper is structured as follows. Section 2 describes the configuration and develops the dynamic model of the PMSG-based wind turbine with qZSI. Section 3 elaborates on the proposed control strategies. Section 4 presents comparative studies along with the simulation and HIL validation results. Section 5 presents the simulation and HIL results. Section 6 presents Practical Design and Stress Analysis. In conclusion, Section 7 summarizes the paper's main findings.

2 Wind Energy Preliminaries

The system's layout, shown in Fig 1, features a PMSG-based wind turbine connected to the grid through a qZSI. The process begins with the PMSG, which converts the wind's kinetic energy into variable-frequency electrical power. This power is then handled by an AC-DC-AC conversion system, which relies on two converters working together: a Machine-Side Converter (MSC) and a Grid-Side Converter (GSC), linked by a DC capacitor. The overall performance of the turbine hinges on the coordinated action of the MSC and GSC. The GSC's role is especially critical, as it is responsible for regulating the PMSG's rotational speed and power output. To do this, the GSC is constructed with its own impedance network, a three-phase Voltage Source Inverter (VSI), and an LCL filter.

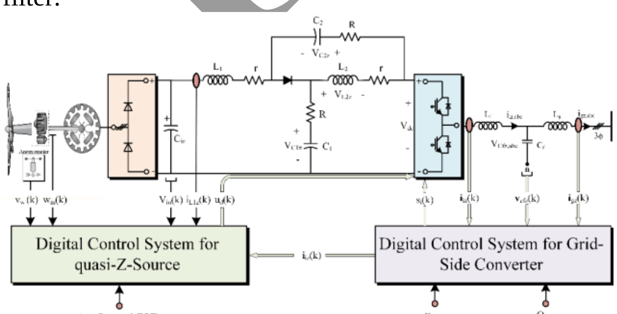

Fig 1. Wind turbine-based PMSG with grid-connected qZSI

In high-power wind energy systems, a diode rectifier with a qZSI is a proven and effective solution for turbines with PMSGs. This approach is well documented in [25]. The diode rectifier offers several key benefits:

1. **Reliability and Robustness**: Diode rectifiers are simple, passive parts that do not need active switching. As a result, they are highly reliable and less likely to fail, which is important in the tough conditions found in wind farms.
2. **Cost and Complexity Reduction**: Removing the controlled rectifier stage reduces parts, simplifies control, and lowers costs. These advantages are especially important for large, multi-megawatt systems.
3. **Compatibility with qZSI MPPT**: The qZSI can boost voltage and track the maximum power point (MPPT) using its shoot-through control. This means there is no need for an extra active rectifier for MPPT.
4. **Grid Code Compliance**: With a well-controlled qZSI and an LCL filter, this setup meets grid harmonic standards like IEEE 1547. This eliminates the need for an active front-end rectifier, particularly at megawatt levels.

The single-stage conversion provided by the qZSI facilitates the power conditioning process while maintaining efficiency and control [9, 25].

2.1 Dynamic Model of Wind Turbine

The rotor blades initially transform kinetic energy into mechanical energy. The kinetic power of the wind P_w passing through a hypothetical area A_T at a velocity v_w is:

$$P_w = \frac{1}{2}\rho_w A_T v_w^3, \quad A_T = \pi r_T^2 \tag{1}$$

Air density (ρ_w) is represented as the mass of air per unit volume (kg/m^3), with A_T denoting the rotor-swept area (m^2), v_w indicating the wind speed (m/s) and r_T representing the blade radius (m). The air's density can change due to altitude, temperature, and humidity. Specifically, at sea level and a temperature of 15 , the air typically displays a density of 1.225 kg/m^3.

Applying the principles of Betz's theory, we can express the mechanical power (P_T) derived from the kinetic power of the wind (P_w) as follows:

$$P_T = P_w \times C_{pT} = \frac{1}{2}\rho_w A_T v_w^3 C_{pT} \tag{2}$$

The power coefficient of rotor blades, denoted as C_{pT}, determines the proportionate increase in extraction of power represented by P_T. Betz stated that the highest achievable C_{pT} value is 0.593. In the realm of high-power wind turbines, the C_{pT} values typically fall within the range of 0.32 to 0.52 for newer models. Information on

C_{pT} values for different commercial wind turbines can be referenced in [26]. The definition of C_{pT} in relation to turbine coefficients C_{T1} through C_{T7} is provided below:

$$C_{pT} = C_{T1}\left(\frac{C_{T2}}{\lambda_I} - C_{T3}\beta_T - C_{T4}\beta_T^2 - C_{T5}\right) e^{\frac{C_{T6}}{\lambda_I}} + C_{T7}\lambda_T \quad (3)$$

The pitch angle, denoted by β_T, can be modified by the pitch control system, while λ_T represents the optimal tip-speed ratio (TSR). The value of λ_T is determined as follows:

$$\lambda_T = \lambda_T^{op} = \frac{\omega_T r_T}{v_{w,R}} \quad (4)$$

Wind turbines that adjust their speed operate at the most efficient Tip Speed Ratio (TSR) value across all wind speeds. The Eq. (3) introduces the intermittent TSR denoted by λ_I, which is linked to λ_T and β_T, as depicted in the following manner:

$$\frac{1}{\lambda_I} = \frac{1}{\lambda_T + 0.08\beta_T} - \frac{0.035}{\beta_T^3 - 1} \quad (5)$$

Fig 2 illustrates how a wind turbine's power output (P_T) and its power coefficient (P_w) change in response to wind speed (v_w). Due to unavoidable aerodynamic losses, the actual power captured by the turbine, P_T, is always lower than the total power available in the wind, P_w.
Three key wind speed thresholds define the turbine's operation:

- Cut-in Speed (3-5 m/s): Below this Speed, the turbine is idle and generates no power.
- Rated Speed (10-15 m/s): Between the cut-in and rated speeds, the power output (P_T) increases cubically with the wind speed. This is the turbine's normal operating range for power generation.
- Cut-out Speed (25-30 m/s): Once the wind exceeds the rated Speed, the turbine's control system actively manages the aerodynamic forces to keep the power output constant at its maximum level. For safety, if the wind speed surpasses the cut-out limit, the turbine shuts down completely[25].

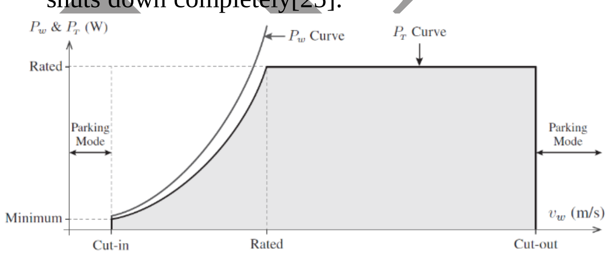

Fig 2. Wind turbine power characteristic curves concerning wind speed [25].

2.2 Dynamic Model of PMSG

PMSG is represented in the synchronous dq-frame through the voltage and electrical torque equations as described in [27]:

$$\begin{cases} i_{dms} &= -\frac{R_{ms}}{L_{dms}} i_{dms} + \frac{\omega_r L_{qms}}{L_{dms}} i_{qms} + \frac{1}{L_{dms}} v_{dms} \\ i_{qms} &= -\frac{\omega_r L_{dms}}{L_{qms}} i_{dms} - \frac{R_{sm}}{L_{qms}} i_{qms} + \frac{1}{L_{qms}} v_{qms} - \frac{\omega_r \psi_r}{L_{qms}} \end{cases} \quad (6)$$

The variables v_{dms} and v_{qms} represent the stator voltages. The quantities i_{dms} and i_{qms} denote the stator currents. Additionally, ψ_r is the magnetic flux, and ω_r is the electrical rotor speed.

The dynamics of the mechanical rotor speed are described as follows:

$$j_m \dot{\omega}_m + B_m \omega_m = T_m - T_e \quad (7)$$

The symbol ω_m represents the rotor mechanical speed in radians per second, while T_e and T_m denote the electromagnetic and shaft mechanical torques in Newton meters, respectively. Additionally, J_m and B_m are the shaft moment of inertia in kilograms per square meter and viscous friction in Newton meters per second. The relationship between the mechanical rotor speed ω_m and the electrical rotor speed ω_r is illustrated as follows:

$$\omega_m = \frac{1}{P_{pm}} \omega_r \quad (8)$$

The symbol P_{pm} denotes the number of pole pairs in an electric machine.

By merging equations (7) and (8), the dynamics of the electrical rotor speed can be expressed as follows:

$$\frac{J_m}{P_{pm}} \dot{\omega}_r = \frac{P_{pm}}{J_m}(T_m - Te) - \frac{B_m}{\omega_r} \quad (9)$$

The electromagnetic torque is acquired in the following manner:

$$T_e = \frac{3P_{pm}}{2}\left[\psi_r i_{qms} - \left(L_{dms} - L_{qms}\right) i_{dms} i_{qms}\right] \quad (10)$$

Upon resolving equations (9) and (10), the behavior of rotor speed is described by the subsequent mathematical expression

$$\dot{\omega}_r = \frac{P_{pm}}{J_m} T_m - \frac{3P_{pm}^2}{2J_m} \psi_r i_{qms} - \frac{3P_{pm}^2}{2J_m}\left(L_{dms} - L_{qms}\right) i_{dms} i_{qms} - \frac{B_m}{J_m} \omega_r \quad (11)$$

2.3 Dynamic Model of qZSI

The qZSI leverages a unique impedance network and a "shoot-through" state to step up its input voltage. As shown in Fig. 3, this creates two fundamental operating modes for the inverter: non-shoot-through and shoot-through [28].

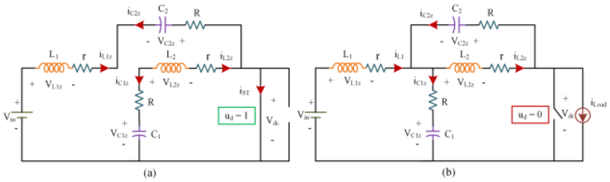

Fig 3. The circuit equivalent to the qZSI network (a) Shoot-through and (b) Non-shoot-through states.

2.3.1 The Generalized Averaging Model of qZSI

The Generalized Averaging Model (GAM) utilizes the complex Fourier series to represent waveforms. This allows for the expression of any periodic variable $\chi(t)$ as:

$$\chi(t) = \sum_{\kappa=-\infty}^{+\infty} \chi_\kappa(t).e^{j\kappa\omega t} \tag{12}$$

the symbol ω represents the fundamental angular frequency, while χ_κ denotes the factor of the κth harmonic, as defined in mathematics.

$$\chi_\kappa(t) = \frac{1}{T}\int_{t-T}^{t} \chi(\tau).e^{-j\kappa\omega\tau}d\tau \tag{13}$$

the period $T = 2\pi/\omega$ aligns with the concept of a sliding average. To provide evidence, we will employ the subsequent notation:

$$\chi_\kappa(t) = \langle\chi\rangle_\kappa(t) \tag{14}$$

Equations (12) and (13) give rise to two essential characteristics. The initial one pertains to the rate of change of the moving average articulated as

$$\frac{d}{dt}\langle\chi\rangle_\kappa(t) = \langle\frac{d}{dt}\chi\rangle_\kappa(t) - j\kappa\omega\langle x\rangle_\kappa(t) \tag{15}$$

Additionally, the second characteristic pertains to the product of the variable:

$$\langle\chi.\vartheta\rangle_\kappa(t) = \sum_i \langle\chi\rangle_{\kappa-i}(t).\langle\vartheta\rangle_i(t) \tag{16}$$

The GAM is derived analytically from the precise topological model using Fourier series expansion. This expansion accounts for the average and first-order harmonic values of the state variables. For AC variables, the primary harmonic ($\kappa = 1$) of the pulsation ω is considered, as outlined in Eq. (15). For DC variables, which exhibit minor variations, only the average value ($\kappa = 0$) is retained.

Regarding the study by [14], it is observed that in the state of equilibrium, the following conditions hold:

$$i_{L_{1z}} - i_{L_{2z}} = 0 \qquad v_{C_{1z}} - v_{C_{2z}} - V_{in} = 0 \tag{17}$$

Therefore, the ultimate dynamic representation of qZSI can be described as follows [28]:

$$\begin{cases} i_{L_{1z}} = -\frac{(r+R)}{L} i_{L_{1z}} - \frac{(1-2d)}{L} v_{C1} + \frac{3R}{2L}(i_{iqz}\beta_q + i_{idz}\beta_d) \\ \quad + \frac{(1-d)}{L} V_{in} \\ \dot{v}_{C_{1z}} = \frac{(1-2d)}{C} i_{L_{1z}} - \frac{3}{2C}(i_{iqz}\beta_q + i_{idz}\beta_d) \\ i_{iqz} = -\omega i_{idz} + \frac{1}{L_f}(2v_{C_{1z}} - V_{in})\beta_q - \frac{r_f}{L_f} i_{iqz} - \frac{1}{L_f} v_{fqz} \\ i_{idz} = \omega i_{iqz} + \frac{1}{L_f}(2v_{C_{1z}} - V_{in})\beta_d - \frac{r_f}{L_f} i_{idz} - \frac{1}{L_f} v_{fdz} \\ \dot{v}_{fqz} = -\omega v_{fdz} + \frac{1}{C_f} i_{iqz} - \frac{1}{C_f} i_{gqz} \\ \dot{v}_{fdz} = \omega v_{fqz} + \frac{1}{C_f} i_{idz} - \frac{1}{C_f} i_{gdz} \\ i_{gqz} = -\omega i_{gdz} + \frac{1}{L_g} v_{fqz} - \frac{r_g}{L_g} i_{gqz} \\ i_{gdz} = \omega i_{gqz} + \frac{1}{L_g} v_{fdz} - \frac{r_g}{L_g} i_{gdz} - \frac{v_{gdz}}{L_g} \end{cases}$$

(18)

The variables d, β_d, and β_q represent control inputs. The eq. (18) is employed for the purpose of designing sliding mode controller.

2.3.2 Small Signal Model of qZSI

In the synchronously rotating (d-q) frame, the Generalized Averaged Model (GAM) of the qZSI can be expressed using the set of equations shown in Eq. (18). Here, $u = [d \quad \beta_q \quad \beta_d]$ represents the input vector, comprising the the dq components of the duty ratio β. Meanwhile,

$x = [i_{L_{1z}} \quad v_{C_{1z}} \quad i_{iqz} \quad i_{idz} \quad v_{fqz} \quad v_{fdz} \quad i_{gdz} \quad i_{gqz}]$ denotes the state vector. Through Eq. (18), the qZSI under consideration can be analyzed from a control perspective akin to a DC-DC converter.

The non-linear model in Eq. (18) is linearized around a steady-state operating point. We define this point using the constant setpoints for the capacitor voltage ($v^*_{C_{1z}}$) and inductor current ($i^*_{L_{1z}}$), while assuming the grid current (i_{gqz}) is zero. Solving the model with its derivatives set to zero provides the remaining steady-state parameters (noted with a subscript 'e'). This completes the fixed point needed for linearization. The subsequent stage involves deriving the linearized form of the Eq. (18) around this equilibrium point, denoted by the symbol e, to indicate deviations from the established stable condition.

$$
\begin{cases}
\widetilde{i_{L_{1z}}} = & -\frac{(r+R)}{L}\widetilde{i_{L_{1z}}} - \frac{(1-2d_e)}{L}\widetilde{v_{C_{1z}}} + \frac{3R\beta_{qe}}{2L}\widetilde{i_{iqz}} \\
& + \frac{3R\beta_{de}}{2L}\widetilde{i_{idz}} + \frac{(2v^*_{C_{1z}}-V_{in})}{L}\tilde{d} + \frac{3Ri_{iqe}}{2L}\widetilde{\beta_q} \\
& + \frac{3Ri_{ide}}{2L}\widetilde{\beta_d} \\
\widetilde{v_{C_{1z}}} = & \frac{(1-2d_e)}{C}\widetilde{i_{L_{1z}}} - \frac{3\beta_{qe}}{2C}\widetilde{i_{iqz}} - \frac{3\beta_{de}}{2C}\widetilde{i_{idz}} - \frac{2i^*_{L_{1z}}}{C}\tilde{d} \\
& - \frac{3i_{iqe}}{2C}\widetilde{\beta_q} - \frac{3i_{ide}}{2C}\widetilde{\beta_d} \\
\widetilde{i_{iqz}} = & -\omega\widetilde{i_{idz}} + \frac{2v^*_{C_{1z}}-V_{in}}{L_f}\widetilde{\beta_q} + \frac{2\beta_{qe}}{L_f}\widetilde{v_{C_{1z}}} - \frac{r_f}{L_f}\widetilde{i_{iqz}} - \frac{1}{L_f}\widetilde{v_{fqz}} \\
\widetilde{i_{idz}} = & \omega\widetilde{i_{iqz}} + \frac{2v^*_{C_{1z}}-V_{in}}{L_f}\widetilde{\beta_d} + \frac{2\beta_{de}}{L_f}\widetilde{v_{C_{1z}}} - \frac{r_f}{L_f}\widetilde{i_{idz}} - \frac{1}{L_f}\widetilde{v_{fdz}} \\
\widetilde{v_{fqz}} = & -\omega\widetilde{v_{fdz}} + \frac{1}{C_f}\widetilde{i_{iqz}} - \frac{1}{C_f}\widetilde{i_{gqz}} \\
\widetilde{v_{fdz}} = & \omega\widetilde{v_{fqz}} + \frac{1}{C_f}\widetilde{i_{idz}} - \frac{1}{C_f}\widetilde{i_{gdz}} \\
\widetilde{i_{gqz}} = & -\omega\widetilde{i_{gdz}} + \frac{1}{L_g}\widetilde{v_{fqz}} - \frac{r_g}{L_g}\widetilde{i_{gqz}} \\
\widetilde{i_{gdz}} = & \omega\widetilde{i_{gqz}} + \frac{1}{L_g}\widetilde{v_{fdz}} - \frac{r_g}{L_g}\widetilde{i_{gd}}
\end{cases}
$$

(19)

The eq. (19) is utilized to design PID and FGS-PID controllers.

3 Control Strategies

The resulting three-phase AC power from the PMSG is immediately converted to DC. This is handled by a diode rectifier along with an input capacitor (C_{in}), which together create the stable DC source voltage (V_{in}) for the qZSI.

The ability to operate a permanent magnet synchronous generator at variable speeds can be accomplished through the utilization of the qZSI, which employs a control scheme based on the current of an inductor. Fig. 4 illustrates the MPPT algorithms that rely on the speed signal feedback (SSF).

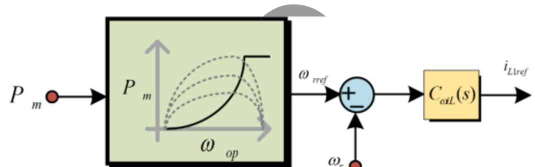

Fig 4. Calculating the reference inductor current based on SSF.

The SSF MPPT algorithm generates a reference speed ω_{rref} by utilizing the measured power P_m.

A proportional-integral (PI) controller is employed to produce the reference inductor current, represented as i_{L1ref}, to keep the generator speed ω_r at its desired value ω_{rref}:

$$i_{L1ref} = \left(k_{pL1} + \frac{k_{iL1}}{s}\right)(\omega_{rref} - \omega_r) \tag{20}$$

The PI controller's proportional gain is denoted by k_{pL1}, while its integral gain is represented by k_{iL1}. The reference inductor current magnitude varies with different wind-speed conditions, allowing for MPPT operation by tracking this variable.

The control system is designed to manage the power injection into the grid. Its primary job is to regulate the active power component while simultaneously providing a specified amount of reactive power. To accomplish this, we have implemented a three-loop cascade control structure. The specific controllers within this structure were designed and tuned using the linearized model from Eq. (19). So, the control system needs to establish a balance of power between the DC and AC components while also preventing both regimes by maintaining an adequate voltage in the DC capacitor $v_{C_{1z}}$. Thus, the initial necessity for power equilibrium translates into regulating the capacitor voltage $v_{C_{1z}}$ to a constant level, guaranteeing the converter's proper functioning. Fig 5 provides a schematic of the proposed control architecture. All key specifications for the qZSI-based wind power system are listed in Table 1. The design of these parameters followed the methodology outlined in reference [29].

Table 1. Design Parameters of the wind power generation system based on qZSI.

PMSG and Rectifying equipment		qZSI and grids	
Rated power	3 □□	□	1 □Ω
Input rectified voltage	1100 □	□	5 □Ω
Stator Resistance	2.01 □Ω	□	17800 □□
Stator Inductance	0.52 □□	□	25.8 □□
Pole Pairs	26	□□	85 □□
Input Capacitors (□□□)	17.8 □□	□□	835 □□
Flux linkage	11.41 □□	□□	3 □□

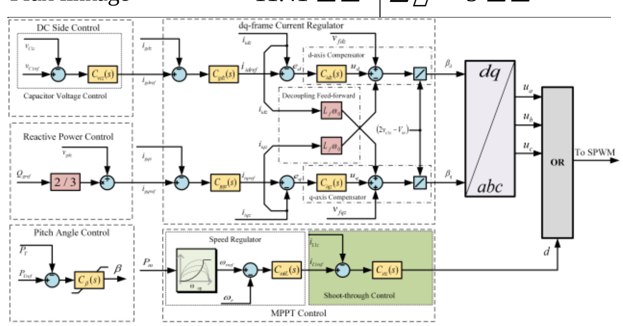

Fig 5. The comprehensive Schematic representation of a grid-connected qZSI control block in Wind turbine-based PMSG.

3.1 Design of classical PI-controller

Assuming steady-state operation and examining the third and fourth components of Eq. (18), we obtain:

$$
\begin{cases}
i_{iqz} & = -\omega i_{idz} + \frac{1}{L_f}(2v_{C_{1z}} - V_{in})\beta_q - \frac{r_f}{L_f}i_{iqz} - \frac{1}{L_f}v_{fqz} \\
i_{idz} & = \omega i_{iqz} + \frac{1}{L_f}(2v_{C_{1z}} - V_{in})\beta_d - \frac{r_f}{L_f}i_{idz} - \frac{1}{L_f}v_{fdz}
\end{cases} \tag{21}
$$

The inner control stage comprises two Proportional-Integral (PI) controllers that regulate the d-q axis currents, i_{idz} and i_{iqz}. The job of these PI controllers is to ensure the measured currents precisely track the reference values provided by the outer control loops. These PI controllers are responsible for producing the compensatory terms (u_{idz} and u_{iqz}). By incorporating the decoupling terms as depicted in eq. (22), autonomous manipulation of i_{idz} and i_{iqz} is achieved, thus enabling control over reactive and active power via the β_q and β_d.

$$\begin{cases} \beta_q = \frac{1}{(2v_{C_{1z}} - V_{in})}\left(u_{iqz} + \omega L_f i_{idz} + v_{fqz}\right) \\ \beta_d = \frac{1}{(2v_{C_{1z}} - V_{in})}\left(u_{idz} - \omega L_f i_{iqz} + v_{fdz}\right) \end{cases} \tag{22}$$

By replacing the symbols β_q and β_d within the third and fourth expressions of Eq. (21), correspondingly, we can infer:

$$\begin{cases} L_f i_{iqz} &= u_{iqz} - r_f i_{iqz} \\ L_f i_{idz} &= u_{idz} - r_f i_{idz} \end{cases} \tag{23}$$

Eq. (23) delineates the characteristics of two separate, initial-order, linear systems. By (23), the variables i_{idz} and i_{iqz} can be managed through the input variables u_{idz} and u_{iqz}, respectively. The schematic diagram depicted in Fig. 5 visually represents the block diagram showcasing the current controllers for the $d-$ and $q-$axis of the qZSI network. Within this diagram, the results of the two corresponding compensators are labeled as u_{idz} and u_{iqz}. The compensator operating along the $d-$axis handles $e_{idz} = i_{idref} - i_{idz}$ and produces u_{idz}. Subsequently, in alignment with (23), u_{idz} influences β_d. Similarly, the compensator functioning along the q-axis processes $e_{iqz} = i_{iqref} - i_{iqz}$ and yields u_{iqz}, which, as per (22), impacts β_q. The qZSI then magnifies β_d and β_q by the factor V_{dc} and produces $d-$ and $q-$axis voltage on the inverter side, thereby regulating i_{idz} and i_{iqz} based on (21). Within the control structure illustrated in Figure 5, all signals for control, feedback, and feed-forward purposes are direct current quantities in equilibrium.

The functions $C_{idz}(s)$ and $C_{iqz}(s)$ have the potential to serve as a basic proportional-integral (PI) compensator that facilitates the ability to follow a DC reference command.

$$C_{idz}(s) = \frac{k_{p1z}s + k_{i1z}}{s} \tag{24}$$

The parameters k_{p1z} and k_{i1z} denote the proportional and integral gains, correspondingly. The s-domain representation for an open loop can be described as an outcome.

$$\ell_{idz}(s) = \left(\frac{k_{p1z}}{L_f s}\right)\frac{s + k_{i1z}/k_{p1z}}{s + r_f/L_f} \tag{25}$$

The pole located at $s = -r_f/L_f$, near the origin, causes a reduction in both the loop gain magnitude and phase at a relatively low frequency. Consequently, the compensator zero at $s = -k_{i1z}/k_{p1z}$ initially cancels out the plant pole, resulting in the loop gain taking the form $\ell_{idz}(s) = k_{p1z}/(L_f s)$. Subsequently, the closed-loop transfer function, denoted as $\ell_{idz}(s)/(1 + \ell_{idz}(s))$, can be expressed as:

$$G_{idz}(s) = \frac{I_{idz}(s)}{I_{idref}(s)} = \frac{1}{\tau_i s + 1} \tag{26}$$

if

$$\begin{cases} k_{p1z} = L_f/\tau_i \\ k_{i1z} = r_f/\tau_i \end{cases} \tag{27}$$

Choosing the PI gains with Eq. (27) is a powerful simplification, as it makes the entire current loop behave like a simple first-order system defined by one parameter: the time constant, τ_i. This makes the tuning process a direct trade-off. While a small τ_i is desirable for a fast response, there is a hard physical limit. The controller's bandwidth, which is $1/\tau_i$, cannot be allowed to approach the qZSI's switching frequency, or the system will become unstable. Therefore, the choice of τ_i is constrained: it must be small enough for good performance, but large enough to keep the bandwidth at least a decade (ten times) below the switching frequency. The converter's switching frequency, denoted as τ_i, is commonly chosen between the range of 0.5 to 5 milliseconds, contingent upon the specific demands of the application. The compensator $C_{idz}(s)$ can also be utilized as the compensator for the q-axis, $C_{iqz}(s)$.

For a given closed-loop time constant ($\tau_i = 1.0\,ms$), Eq. (27) yields the following d- and q-axis compensators:

$$C_{idz}(s) = C_{iqz}(s) = \frac{0.085s + 1}{s} \tag{28}$$

The external loops represent the grid dq current control loops, in which two proportional-integral controllers are employed to govern i_{gdz} and i_{gqz} by the specified reference values from the external control loops. These PI controllers are responsible for producing the reference inverter currents (i_{idref} and i_{iqref}).

The small-signal equations reveal a key symmetry in the system: the transfer function from the d-axis control input ($\square_{\square\square\square}$) to the d-axis grid current ($\square_{\square\square\square}$) is structurally identical to the transfer function from the q-axis control (iq) to the q-axis current ($\square_{\square\square\square}$). These two transfer functions, which we will refer to as $\square^{\square_{\square\square\square}}_{\square_{\square\square\square}}$ and $\square^{\square_{\square\square\square}}_{\square_{\square\square\square}}$, respectively, are both given by the form shown in Eq. (29).

$$\begin{cases} G_{i_{idz}}^{i_{gdz}}(s) = \frac{\iota_{22}s^2+\iota_{21}s+\iota_{20}}{\varrho_{24}s^4+\varrho_{13}s^3+\varrho_{22}s^2+\varrho_{21}s+\varrho_{20}} \\ G_{i_{iqz}}^{i_{gqz}}(s) = \frac{\iota_{22}s^2+\iota_{21}s+\iota_{20}}{\varrho_{24}s^4+\varrho_{23}s^3+\varrho_{22}s^2+\varrho_{21}s+\varrho_{20}} \end{cases} \tag{29}$$

To explore the process of tracking time-varying commands more deeply, one can analyze the closed-loop grid current control system of qZSI by examining its transfer function.

$$G_{gdz} = \frac{I_{gdz}(s)}{I_{gdref}(s)} = \frac{\ell_{gdz}(s)}{1+\ell_{gdz}(s)} \tag{30}$$

where the loop gain $\ell_{gdz}(s)$ is specified as follow:

$$\ell_{gdz}(s) = C_{gdz}(s)G_{i_{idz}}^{i_{gdz}}(s) \tag{31}$$

$C_{gdz}(s)$ and $C_{gqz}(s)$ can act as a straightforward PI compensator in order to facilitate the DC reference command tracking. Let

$$C_{gdz}(s) = \frac{k_{p2z}s+k_{i2z}}{s} \tag{32}$$

The selection of parameters for PI compensators in the i_{gdz} control loop is determined by the lower bandwidth of this loop compared to the i_{idz} control loop. The compensators for the d- and q-axis are as follows:

$$C_{gdz}(s) = C_{gqz}(s) = \frac{226.1}{s} \tag{33}$$

The system is stable, with a phase margin of 90° and a closed-loop control system bandwidth of $226\ rad/s$.

To regulate the voltage across a capacitor, a PI controller is utilized to control the value of $v_{C_{1z}}$ in order to track its reference value and produce the desired grid currents (I_{gdref}).

As per the small-signal equations, the transfer system is represented as $G_{i_{gdz}}^{v_{C_{1z}}}$ in eq. (34) describes the relationship between the input i_{gdz} and the d-axis grid current $v_{C_{1z}}$.

$$G_{i_{gdz}}^{v_{C_{1z}}}(s) = -\frac{\iota_{33}s^3+\iota_{32}s^2+\iota_{31}s+\iota_{30}}{\varrho_{36}s^6+\varrho_{35}s^5+\varrho_{34}s^4+\varrho_{33}s^3+\varrho_{32}s^2+\varrho_{31}s+\varrho_{30}} \tag{34}$$

Examine how the transfer function regulates the capacitor voltage on the DC side of a closed-loop qZSI system.

$$G_{vcz} = \frac{V_{C_{1z}}(s)}{V_{C1ref}(s)} = \frac{\ell_{vcz}(s)}{1+\ell_{vcz}(s)} \tag{35}$$

where the loop gain $\ell_{vcz}(s)$ is specified as

$$\ell_{vcz}(s) = C_{vcz}(s)G_{i_{gdz}}^{v_{C_{1z}}}(s) \tag{36}$$

The transfer function $C_{vcz}(s)$ can act as a basic proportional-integral (PI) compensator to assist in pursuing a DC reference command tracking.

$$C_{vcz}(s) = \frac{k_{p3z}s+k_{i3z}}{s} \tag{37}$$

When designing the PI compensator for the outer voltage control loop ($v_{C_{1z}}$), we follow a key principle of cascaded control: outer loops must be significantly slower than inner loops. This creates a clear bandwidth hierarchy for the system. As specified for this design, the $v_{C_{1z}}$ loop is the slowest, the grid current (i_{gdz}) loop is faster, and the d-axis current (i_{idz}) loop is the fastest of all. Based on this principle, the compensator we use is:

$$C_{vcz}(s) = -\frac{6s+800}{s} \tag{38}$$

The control system with feedback operates within a bandwidth of $5.31\ rad/s$.

Fig 5 shows the feedback loop designed to regulate the input inductor current. The measured inductor current is compared to its reference value, and the resulting error signal is fed into a Proportional-Integral (PI) controller. The controller processes this error to calculate the necessary shoot-through duty cycle (□). To ensure optimal performance, the PI controller is tuned using the system's transfer function, □□□□1□, as defined in Eq. (39).

$$G_d^{i_{L1z}}(s) = \frac{\iota_{47}s^7+\iota_{46}s^6+\iota_{45}s^5+\iota_{44}s^4+\iota_{43}s^3+\iota_{42}s^2+\iota_{41}s+\iota_{40}}{\varrho_{48}s^8+\varrho_{47}s^7+\varrho_{46}s^6+\varrho_{45}s^5+\varrho_{44}s^4+\varrho_{43}s^3+\varrho_{42}s^2+\varrho_{41}s+\varrho_{40}} \tag{39}$$

Examine the closed-loop regulation of inductor current by analyzing its transfer function.

$$G_{stz} = \frac{I_{L_{1z}}(s)}{I_{L1ref}(s)} = \frac{\ell_{stz}(s)}{1+\ell_{stz}(s)} \tag{40}$$

the loop gain $\ell_{stz}(s)$ is given by

$$\ell_{stz}(s) = C_{stz}(s)G_d^{i_{L_{1z}}}(s) \tag{41}$$

The regulator's transfer function $C_{stz}(s)$ is defined as

$$C_{stz} = \frac{K_{p4z}s+K_{i4z}}{s} \tag{42}$$

The selection of the parameters for the PI compensator to control $i_{L_{1z}}$ is determined by ensuring a suitable phase margin while ensuring that the control loop bandwidth exceeds that of the $v_{C_{1z}}$control loop. Consequently, the compensator can be derived in the following manner:

$$C_{stz}(s) = \frac{0.0022}{s} \tag{43}$$

The system displays stability, with a phase margin of $62.7°$ and a closed-loop control system bandwidth of $19.34\ rad/s$.

The reference for the q-axis current control loop is determined using Eq. (44) in the dq reference frame. Under the assumption of a stiff grid where the grid voltage

(v_{gdz}) remains constant, regulating the q-axis grid current (i_{qgz}) is equivalent to controlling the reactive Q_g [29].

$$\begin{cases} P_g &= \frac{3}{2} v_{dgz} i_{dgz} \\ Q_g &= -\frac{3}{2} v_{dgz} i_{qgz} \end{cases} \tag{44}$$

The pitch angle of blade (β) is adjusted by the wind turbine's pitch angle controller to decrease P_T, which limits the power produced by the wind turbine when wind speeds are higher than the rated value [9].

3.2 Sliding Mode Control of Inductor Current

SMC is particularly suitable for the qZSI inductor current loop due to three fundamental considerations. Firstly, the qZSI has two distinct topological states: the shoot-through state and the non-shoot-through state. This variable structure is naturally compatible with the discontinuous nature of the control action in SMC. Secondly, the sliding surface in Eq. (45) has the advantage of combining both inductor current error and capacitor voltage error, utilizing the inherent coupling relationship between the two to simultaneously regulate the inductor current. Finally, SMC has the advantage of robustness against matched disturbances and parameter changes. This is particularly important as the wind speed changes continuously, thereby altering the operating point. The invariance principle of SMC ensures that the system dynamics, once the system is on the sliding surface, depend only on the choice of the sliding surface and are completely immune to uncertainties. This is in direct correspondence with the experimental results where the capacitor voltage ripple and THD have been reduced.

In this section, we replace the PI controller for the inductor current with a more robust Sliding Mode Controller (SMC). The design process for an SMC has two main steps, the first and most critical being the selection of the sliding-mode surface. This surface defines the ideal trajectory for the system's state variables. The controller's primary job is to force the system onto this surface and maintain it there, which is crucial for satisfying the sliding-mode reaching condition and ensuring stable control.

In this manuscript, the concept of the sliding surface is described in the following manner:

$$S_{stz} = e_{i_{L_{1z}}} + \gamma e_{v_{C_{1z}}} \tag{45}$$

where $e_{i_{L1z}} = i_{L1ref} - i_{L_{1z}}$, $e_{v_{C_{1z}}} = v_{C1ref} - v_{C_{1z}}$ and $\gamma = \frac{RC}{L}$.

The rate of change of the switching functions can be represented using Equations (45) and (18). This formula can be expressed as follows:

$$\dot{S}_{stz} = i_{L1ref} - i_{L_{1z}} - \gamma \dot{v}_{C_{1z}} \tag{46}$$

The sliding surface in Equation (45) uses both the inductor current error and the capacitor voltage error. This approach is based on the coupled dynamics of the quasi-Z-source inverter. In the qZSI network, the inductor current $i_{L_{1z}}$ and capacitor voltage $v_{C_{1z}}$ are linked by the circuit's shoot-through and non-shoot-through states. If only the inductor current is regulated and capacitor voltage variations are ignored, unwanted DC-link voltage deviations may occur, affecting system stability and power quality.

The chosen surface S_{stz}, together with γ, keeps a balance between current tracking and voltage regulation. Using several variables helps the controller maintain the energy balance in the impedance network and respond well to sudden changes and outside disturbances. This method matches established sliding-mode control techniques for impedance-source converters, where using multiple state variables has been shown to make the system more robust and improve its dynamic performance [18, 20, 30].

By adopting this coupled sliding surface, the proposed SMC not only achieves precise inductor current tracking but also inherently limits capacitor voltage stress, contributing to the overall reliability of the 3 MW wind-energy conversion system.

This study will utilize a control input comprising a comparable control regulation and a discretized component. The comparable control regulation establishes $\dot{S}_{stz} = 0$.

$$d_{eq} = \frac{L i_{L1ref} + r i_{L_{1z}} + v_{C_{1z}} - V_{in}}{2 v_{C_{1z}} - V_{in} - 2R i_{L_{1z}}} \tag{47}$$

An additional discrete term of $-Ksgn(S_{stz})$ is introduced into the equivalent disturbance input d_{eq} to counteract unforeseen disturbances in a system, such as unaccounted dynamics or parameter deviations. This inclusion works towards improving the system's robustness. The resultant control input is labeled as d.

$$d = d_{eq} + Ksgn(S_{stz}) \tag{48}$$

The switching gain parameter, denoted as K, is a key element in the SMC system. It is a positive numerical value that influences the system's robustness. A higher value of K can enhance the system's robustness, but an excessively high value can lead to increased chattering, which is undesirable. Therefore, selecting an appropriate value for K is crucial in the design of Sliding Mode Control (SMC). The choice of K impacts on the ST ratio, with a larger value of K resulting in a noticeable increase in inductor current ripple.

Selecting the Lyapunov function $V = \frac{1}{2} S_{stz}^2$ and computing its derivative leads to

$$
\begin{aligned}
\dot{V} &= S_{stz}\dot{S}_{stz} \\
&= S_{stz}\Big(i_{L1ref} - \tfrac{V_{in}-ri_{L_{1z}}-V_{C_{1z}}}{L} \\
&\quad - \tfrac{2V_{C_{1z}}-V_{in}-2Ri_{L_{1z}}}{L}(d_{eq} + Ksgn(S_{stz})) + \phi\Big) \\
&= S_{stz}\Big(\tfrac{2V_{C_{1z}}-V_{in}-2Ri_{L_{1z}}}{L}Ksgn(S_{stz}) + \phi\Big)
\end{aligned} \tag{49}
$$

The unknown disturbance ϕ comprises primarily parameter deviation and unmodeled dynamics. It is assumed that ϕ is limited, with $\phi_{max} < \eta$. Certain conditions need to be satisfied to guarantee the sliding condition.

$$K > \frac{\eta L}{2V_{C_{1z}}-V_{in}-2Ri_{L_{1z}}} > 0 \tag{50}$$

3.3 Fuzzy Gain Scheduling-PID Controller of Inductor Current

The widely used PID controllers dominate the industrial control domain because of the simplicity of the control algorithm and the fixed switching frequency. However, the gains of the controller cannot be varied, which is a drawback in the context of the wide range of operation of wind turbines. The FGS controller overcomes the drawback of the traditional PID controller by relating the gains of the controller to the error and the derivative of the error using heuristic knowledge of the system. In the context of qZSI current control, the FGS-PID controller represents a compromise between the simplicity of the control algorithm of the traditional controller and the complexity of nonlinear control algorithms. Although the FGS-PID controller cannot offer the robustness of the sliding mode control algorithm, it can be implemented on the existing hardware of the system, which represents a significant advantage of the controller.

This segment employs FGS-PID to calculate a shoot-through duty cycle (d). As depicted in Fig. 6, the fuzzy inference block consists of a fuzzy interface, rule base, fuzzy inference mechanism, and defuzzification interface [32]. Fuzzification plays a crucial role in FGS-PID controllers, as it facilitates the handling of system nonlinearities and uncertainties. Fuzzification entails the representation of system inputs and outputs as fuzzy sets, thereby enhancing the controller's ability to interpret the system more flexibly and robustly. Nonetheless, FGS-PID controllers can adapt their real-time parameters according to the system's current condition, which enhances their ability to effectively manage these nonlinearities and uncertainties.

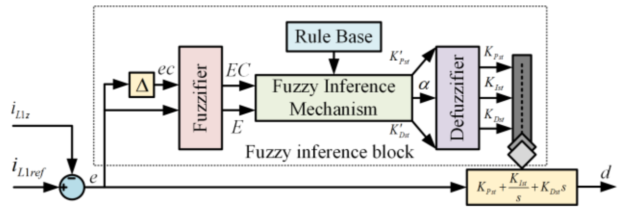

Fig 6. Structure diagram of inductor current control based on fuzzy inference

The representation of the transfer function for a PID controller is outlined as follows:

$$C_{stz}(s) = K_{Pst} + \frac{K_{Ist}}{s} + K_{Dst}s \tag{51}$$

The values K_{Pst}, K_{Dst}, and K_{Ist} represent the proportional, derivative, and integral gains, respectively. Another relevant alternative representation of the PID controller is:

$$C_{stz}(s) = K_{Pst}\left(1 + \frac{1}{T_{Ist}s} + T_{Dst}s\right) \tag{52}$$

The relationship between the derivative and integral time constants, denoted as T_{Ist} and T_{Dst} respectively, can be expressed as follows: $T_{Ist} = K_{Pst}/K_{Ist}$ and $T_{Dst} = K_{Dst}/K_{Pst}$.

The tuning of PID gains is conducted in real-time concerning the fuzzy inference and knowledge base. Subsequently, the PID controller produces the control signal. The FGS-PID controller is distinguished by three corrective actions, namely K_{Pst}, K_{Dst}, and K_{Ist}. It is presupposed that K_{Pst} and K_{Dst} fall within specified ranges $[K_{Pst.min}.K_{Pst.max}]$ and $[K_{Dst.min}.K_{Dst.max}]$ respectively. A linear transformation is applied to normalize K_{Pst} and K_{Dst} to a range from zero to one for ease of use.

$$\begin{cases} K'_{Pst} = \dfrac{(K_{Pst}-K_{Pst,min})}{(K_{Pst,max}-K_{Pst,min})} \\ K'_{Dst} = \dfrac{(K_{Dst}-K_{Dst,min})}{(K_{Dst,max}-K_{Dst,min})} \end{cases} \tag{53}$$

The scheme introduced in the study calculates PID parameters by considering the current value e error and its initial difference Δe. Determining the integral time constant is based on the derivative time constant, thus establishing a relationship between the two.

$$T_{Ist} = \alpha T_{Dst} \tag{54}$$

The integral gain is obtained through an acquisition process.

$$K_{Ist} = \frac{K_{Pst}}{\alpha T_{Dst}} = \frac{K_{Pst}^2}{\alpha K_{Dst}} \tag{55}$$

The error (e) of the inductor current and the rate of change of error (ec) directly indicates the state of the qZSI. Thus, they are chosen as input parameters for the fuzzy inference unit. Upon completion of the fuzzification, fuzzy inference mechanism, and defuzzification processes, the parameters K'_{Pst}, K'_{Dst}, and α required for computing the ultimate PID gains are determined. The input parameter is classified into seven fuzzy sets, which are denoted as: "Negative Big" (NB), "Positive Big" (PB), "Negative Middle (NM)," "Positive Middle" (PM), "Negative Small" (NS), "Positive Small (PS)", and "Zero" (ZE). The output parameters K'_{Pst} and K'_{Dst} are categorized into two fuzzy sets, specifically: "Small (S)" and "Big (B)."

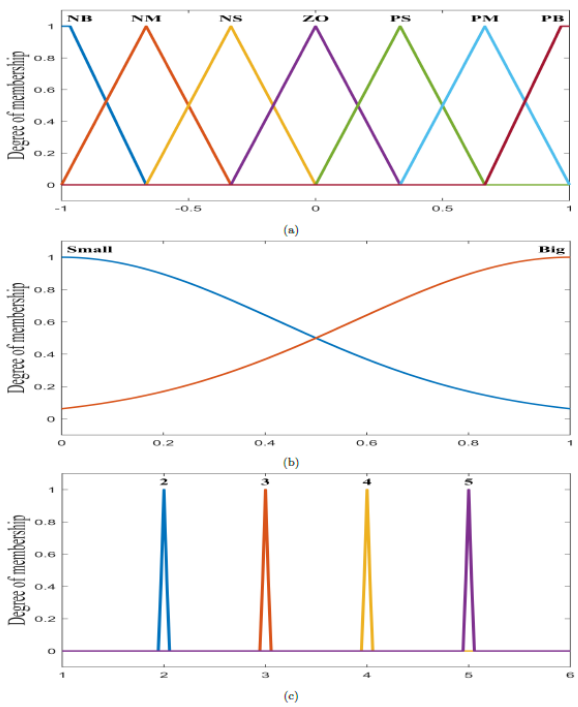

Fig 7. membership function of (ec) E and EC; (kpd)K'_{Pst} and K'_{Dst}; (alpha) α.

Fig 7 defines the membership functions for the fuzzy controller's inputs and outputs.

Fuzzy rules play a crucial role in the current control framework of the inductor outlined in this study, which comprises a sequence of fuzzy conditional statements. The fuzzy inference process incorporates error and its rate of change as variables, which are then processed to generate fuzzy outputs K'_{Pst}, K'_{Dst}, and α based on the established fuzzy rules. The application of fuzzy logic, presented in IF-THEN format, is articulated as follows:

$$\text{if } \mathrm{E = NS \text{ and } EC = N, \text{ then } K'_{Pst} = Bg} \tag{56}$$

E, EC, and K_{Pst} represent fuzzy sets that are defined on fuzzy input and output domains. Consequently, a collection of rules, as depicted in Table 2, can be utilized to adjust the proportional gain (K'_{Pst}). Tables 3 and 4 present the tuning guidelines for K'_{Dst} and α, respectively.

Table 2. Fuzzy Tuning rules for K'_{Pst}

		EC						
		NB	NM	NS	ZO	PS	PM	PB
E	NB	Bg	Bg	Bg	Bg	Bg	Bg	Bg
	NM	Sl	Bg	Bg	Bg	Bg	Bg	Sl
	NS	Sl	Sl	Bg	Bg	Bg	Sl	Sl
	ZO	Sl	Sl	Sl	Bg	Sl	Sl	Sl
	PS	Sl	Sl	Bg	Bg	Bg	Sl	Sl
	PM	Sl	Bg	Bg	Bg	Bg	Bg	Sl
	PB	Bg	Bg	Bg	Bg	Bg	Bg	Bg

Table 3. Fuzzy Tuning rules for K'_{Dst}

		EC						
		NB	NM	NS	ZO	PS	PM	PB
E	NB	Sl	Sl	Sl	Sl	Sl	Sl	Sl
	NM	Bg	Bg	Sl	Sl	Sl	Bg	Bg
	NS	Bg	Bg	Bg	Sl	Bg	Bg	Bg
	ZO	Bg	Bg	Bg	Bg	Bg	Bg	Bg
	PS	Bg	Bg	Bg	Sl	Bg	Bg	Bg
	PM	Bg	Bg	Sl	Sl	Sl	Bg	Bg
	PB	Sl	Sl	Sl	Sl	Sl	Sl	Sl

Table 4. Fuzzy Tuning rules for α

		EC						
		NB	NM	NS	ZO	PS	PM	PB
E	NB	2.0	2.0	2.0	2.0	2.0	2.0	2.0
	NM	3.0	3.0	2.0	2.0	2.0	3.0	3.0
	NS	4.0	3.0	3.0	2.0	3.0	3.0	4.0
	ZO	5.0	4.0	3.0	3.0	3.0	4.0	5.0
	PS	4.0	3.0	3.0	2.0	3.0	3.0	4.0
	PM	3.0	3.0	2.0	2.0	2.0	3.0	3.0
	PB	2.0	2.0	2.0	2.0	2.0	2.0	2.0

The defuzzification procedure involves inputting the aggregate output fuzzy set and generating a singular numerical result. While fuzziness aids in assessing rules

at various stages, the ultimate goal is to have a solitary numerical value for each variable. Nonetheless, a fuzzy set's aggregate encompasses a spectrum of output values, necessitating defuzzification to derive a singular output value from the set. This study uses the centroid method as the technique for defuzzification.

4 Comparative Study

A comparative study in table (5) comprehensively compares the proposed control strategies with conventional methods. The table clearly demonstrates that the proposed cascade control strategies achieve the lowest grid currents THD even in the worst control scenario (conventional PID controller). Among the three control approaches, the SMC control strategy offers the lowest possible THD and a small ripple in DC capacitor voltage. This thorough comparison instills confidence in the research. Conversely, few studies have utilized the grid-connected qZSI structure in wind power applications.

Table 5. Comparison of traditional and proposed control strategies for wind turbine based the three-phase grid-connected qZSI

Control methods	Advantages	Drawbacks
Predictive control [23, 24, 31-33]	• Harmonic Reduction. • Dynamic Performance. • Reduce switching frequency. • Improved Power Quality.	• Complexity in design. • Sensitivity to parameter changes. • Design Challenges. • Computational Demand.
Sliding mode control [18, 20, 30]	• Robustness and dynamic response • Optimal performance. • Decrease the switching frequency. • Enhanced power quality.	• Intricate mathematical modeling. • Potential for chattering. • Complexity in implementation. • Has not been used in WECS.
Direct power control [34]	• Straightforward control structure. • Fast dynamic response. • Disturbance rejection	• Need for switching noise filters. • Influenced by parametric variations. • High THD. • Dynamic switching frequency.
PI based controller [11-13, 35, 36]	• Ensures seamless implementation. • fixed switching frequency.	• Needs a dynamic model. • Intricate cascade PI tuning.
Proposed methods	• High Dynamic Accuracy. • Simple design of cascaded PIs. • Simplicity in design of SMC. • Good reference tracking. • Low THD in grid side currents. • Stability in disturbance conditions.	• Not easy to implement FGS-PID.

5 Simulation Results

In this section, the dynamic efficacy of the three proposed control methodologies is systematically assessed and juxtaposed in the context of variations in wind velocity and reactive power reference, in addition to a voltage sag as a perturbation within the grid. Furthermore, an experimental Hardware-in-the-Loop HIL) validation of the proposed control methodologies is delineated in this segment. All controller parameters repesent in Table 6:

Table 6: Controller parameters of each control methods

Control methods	C_{stz}		$C_{\square}$		$C_{\square iL}$		C_{vcz}		$C_{gdz} = C_{gqz}$		$C_{idz} = C_{iqz}$	
	parameters	value	parameters	value	parameters	value	parameters	value	parameters	value	parameters	value
PID	K_{p4z}	0	K_{p6z}	1.5	K_{p5z}	0.5	K_{p3z}	-6	K_{p2z}	0	K_{p1z}	0.085
	K_{i4z}	0.0022										
FGS	Membership function											
SMC	K	0.007	K_{i6z}	6	K_{i5z}	10	K_{i3z}	-800	K_{i2z}	226.1	K_{i1z}	1
	$\square$	0.6899										

5.1 Long Simulation with Variable Wind Speed

Our research utilizes the Matlab/Sim-Power Systems toolbox for carrying out simulations and thoroughly assessing the effectiveness of the suggested control strategies. A thorough examination evaluates the effectiveness of the GSC's PI-controller, SMC, and FGS-PID in varying wind conditions. The specifications of the PMSG can be found in Table 1. The PI-controller parameters of the GSC are established using the methodologies outlined in Section 2. The GSC relies on the proposed control method to manage the capacitor voltage ($v_{C_{1z}}$) of the overall qZSI and maintain a unity power factor.

Fig 1 illustrates the block diagram of the proposed system. The wind turbine model calculates this configuration's mechanical torque by analyzing the wind velocity and generator rotor speed. The PMSG converts the mechanical torque into active electric power, which is then delivered to the grid via a three-phase diode-bridge rectifier and qZSI. The system for generating wind energy is assumed to be linked to the utility grid at a low voltage of $690V$ and operates under conditions typical of our specified target area. The system operates at a switching frequency of 10800 Hz, with an output frequency of 60 Hz.

The performance of the three controllers is evaluated when subjected to changes in wind speed, as depicted in Fig 8.

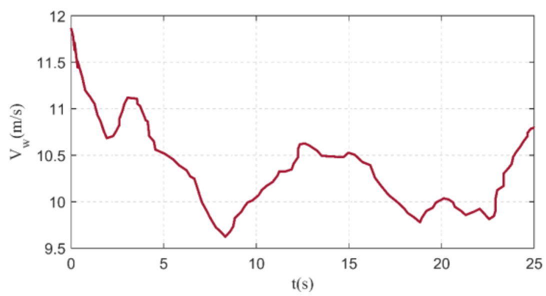

Fig 8. wind speed variation.

The PMSG functions in a mode of maximum power point tracking, whereby the control of its electrical rotational speed is predicated on the optimal active power curve. Variations in wind speed lead to changes in the electromagnetic torque and DC inductor current. The $q-$axis grid current is kept constant at zero to maintain a unity power factor. The PI-controller, SMC, and FGS-PID simulation results are depicted in Fig 9. This illustration showcases the waveforms of various parameters, such as the dc-link voltage (V_{dclink}), capacitor voltage ($v_{C_{1z}}$), inductor current ($i_{L_{1z}}$), shoot-through control signal, inverter phase currents (i_{iabc}), grid phase currents (i_{gabc}), and electrical rotational speed (ω_r). In steady-state operation with a constant wind speed of 10 m/s, it is found that all three controllers regulate the capacitor voltage within ±1% of the reference voltage, which is set to 1400V, while keeping the total harmonic distortion (THD) of the grid current under 3%. Quantitative differences between the three controllers are significant, as it is found that, among the three, SMC has the smallest ripple voltage, equal to ±5V (0.35%), while it also has the lowest THD, equal to 1.8%, as compared to a ripple voltage of ±13V (0.92%) and a THD of 3% for the PI controller. The FGS-PID controller has a ripple voltage of ±10V (0.71%) and a THD of 2.5%. The actual values of capacitor voltage, electrical rotational speed, inductor current, and LCL currents closely follow the reference values. A comparison of the results of the three controllers is presented in Table 6, revealing that SMC delivers superior performance.

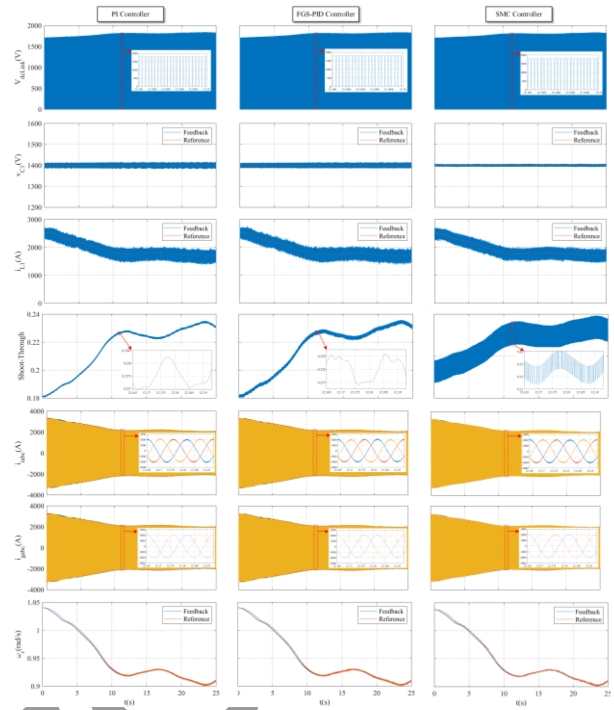

Fig 9. Obtained long simulation results of the 3 MW WECS based three phase qZSI using the conventional PI and FGS-PID and the SMC controllers, where the dc-link voltage (V_{dclink}) with zoom for some switching cycle, the inductor current ($i_{L_{1z}}$), the capacitor voltage ($v_{C_{1z}}$), the shoot-through control signal, the inverter phase currents (i_{iabc}), the grid phase currents (i_{gabc}) and electrical rotational speed (ω_r) are shown from top to bottom.

The conventional PI and FGS-PID and the SMC controllers, where the dc-link voltage (V_{dclink}) with zoom for some switching cycle, the capacitor voltage ($v_{C_{1z}}$), the inductor current ($i_{L_{1z}}$), the shoot-through control signal, the inverter phase currents (i_{iabc}), the grid phase currents (i_{gabc}) and electrical rotational speed (ω_r) are shown from top to bottom.

Table 7. Comparsion between the three controllers' performance.

	PI	FGS-PID	SMC
$v_{C_{1z}}$ ripple	$\pm$ 13V (0.92%)	$\pm$ 10V(0.71%)	$\pm$ 5V(0.35%)
Grid current THD	$\leq$ 3%	$\leq$ 2.5%	$\leq$ 1.8%

5.2 Short Simulation Involving Alterations in Reactive Power Setpoint and Grid Voltage Sag

This simulation assesses the performance of three proposed control systems during potential short-term conditions, including variations in the reactive power setpoint directed by the system operator and a grid voltage sag of 0.70 p.u at 3.5 second lasting for 50 milliseconds.

Fig 10 delineates the grid's reactive and active power ascertained within this case study, wherein the system is modeled under the subsequent operational parameters: 1) a constant wind velocity is posited at 12 m/s; 2) the operational requirements of the system operator stipulate an active power output of 2.7 MW; 3) The system functions at a unity power factor, where reactive power is effectively zero, except for the interval ranging from 2 to 3 seconds, during which the system operator requisitions a reactive power of -0.56 $perunit$, corresponding to -1.7 $MVar$. About the voltage sag phenomenon, the system functions with an active power level of 2.7 MW and exhibits a unity power factor immediately preceding the disturbance. During the 0.70 p.u. grid voltage sag, the active power increases to 3.1 MW for the PI controller, 2.95 MW for FGS-PID, and 2.9 MW for SMC. This increase is attributed to the reduced grid voltage, where the controllers maintain the injected currents, resulting in an increased power output due to the reduced voltage. The greater overshoot for the PI controller (~41.1%) compared to SMC (~31.7%) is attributed to the reduced phase margin (62.7°) and the absence of the disturbance rejection characteristic for the linear control strategy.

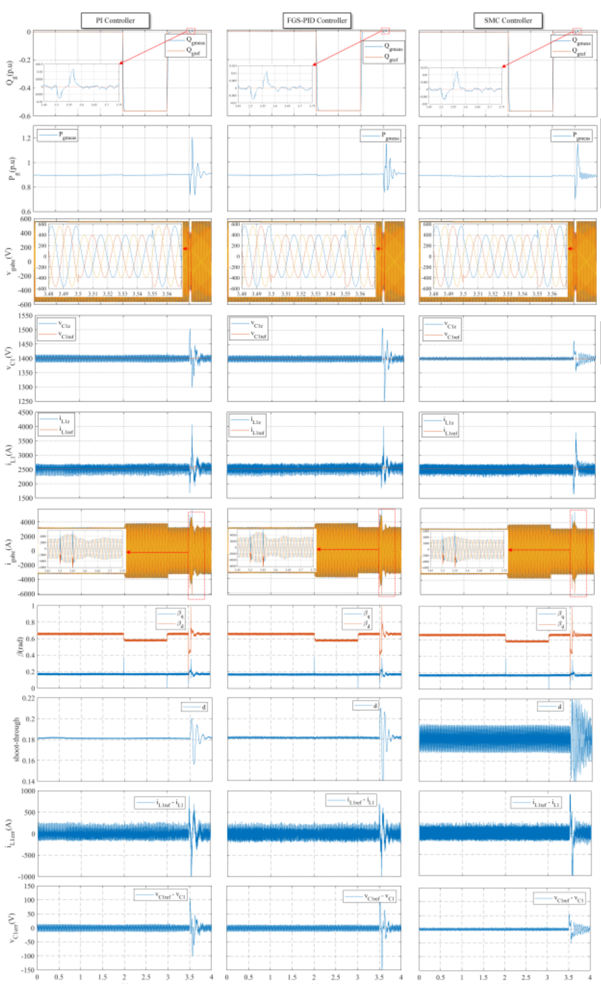

Fig 10. Obtained short simulation results of the 3 MW WECS based three phase qZSI using the conventional PI and FGS-PID and the SMC controllers, where the measured grid reactive power (Q_g) and active power (P_g), the grid voltages (v_{gabc}), the inductor current ($i_{L_{1z}}$), the capacitor voltage ($v_{C_{1z}}$), grid currents (i_{gabc}), the modulation indices (□□.□), shoot through duty cycle (d), the inductor current error signal (□□1□□□) and the capacitor voltage error signal (□□1□□□) are shown from top to bottom.

After the disturbance is resolved and the grid voltage is restored, the active power returns to its normal level and remains stable. The PI and FGS-PID exhibit diminished variability in the transient phase and reach the conditions prior to the fault more efficiently than the SMC.

Fig 10 depicts the influence of voltage sag on the grid voltage (v_{gabc}) and corresponding current (i_{gabc}). The transient behavior of the grid current noted for the PI and FGS-PID is marginally more pronounced than that observed in the SMC controllers. Regarding the DC capacitor voltage (v_{C1z}) depicted in this figure, minimum ripple is evident before the fault event with the SMC controller, and after that, this controller fluctuates more. Ultimately, stabilizing the grid current after the fault signifies that the wind turbine's operational control is adequate once the grid voltage has been restored.

The results indicated the exact tracking capability of the reactive power command. There was very little, almost no, overshoot, and an extremely fast settling time. Also presented are the control command signals □□ and □□, which exhibit smooth responses and modulate values that remain bounded throughout dynamic events. Finally, during the disturbance, the shoot-through duty cycle □ is stable and well-regulated, preventing excessive voltage and/or current stresses on the electrical power devices, and enabling the quasi-Z-source network to function properly.

Overall, the short-term simulation results show that the proposed control schemes effectively reject disturbances, effectively decouple active and reactive power, and exhibit very good transient performance for grid-tied applications.

5.3 Experimental HIL Results

This section delineates the empirical findings that facilitate evaluating and juxtaposing the real-time efficacy of the three proposed control frameworks.

Fig 11 illustrates the experimental HIL configuration established to corroborate the simulation outcomes. The power generation facility operates in real-time within a

FPGA[1]-based simulation apparatus. The control architecture runs on a Texas Instruments Sitara AM5728 development board, while a desktop computer is employed to observe the relevant signal parameters. Lastly, the data depicted in this section are acquired through a SIGLENT SDS1202X-E oscilloscope, which quantifies the inputs and outputs from both real-time simulation environments.

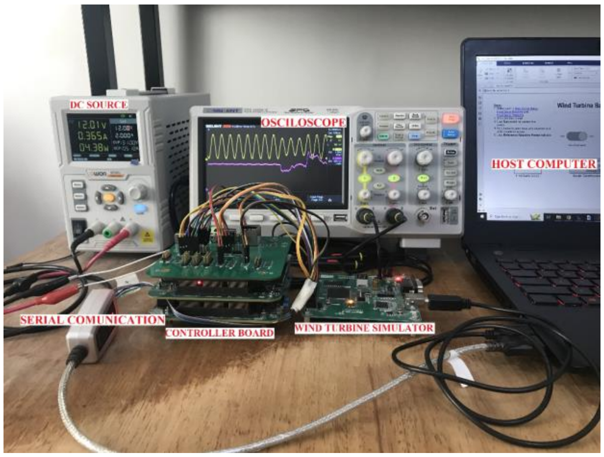

Fig 11. The proposed HIL configuration

As shown in Fig 12, the results from the experimental setup validate the simulation findings and support the previously reported analysis. This figure shows that the active and reactive powers adequately track the operator's command using three control structures. This indicates that the control systems' proper operation has been implemented. Besides, the capacitor voltage (v_{C1z}), phase-A grid current (i_{ga}), DC inductor current (i_{L1z}) and phase-A grid voltage are also represented in this figure. When active and reactive powers change, the SMC shows similar responses to the PI and FGS-PID controllers, with no significant differences.

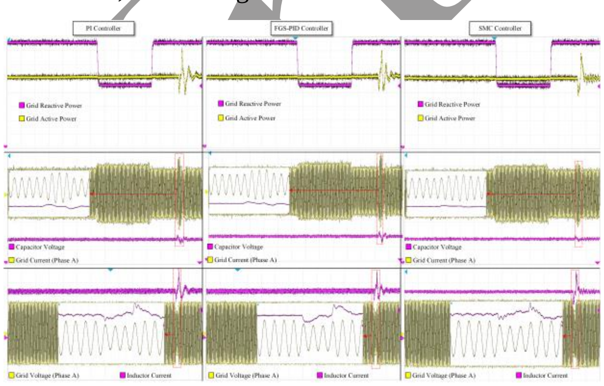

Fig 12. Obtained experimental HIL results of the 3 MW WECS based three phase qZSI using the conventional PI and FGS-PID and the SMC controllers, where the measured grid reactive power (Q_g) and active power (P_g), the grid current (i_{ga}) and capacitor voltage ($v_{C_{1z}}$) with zoom for some switching cycles, the inductor current ($i_{L_{1z}}$) and grid voltage (v_{ga}) are shown from top to bottom.

The outcomes of the experimental setup, illustrated in Fig. 12, show the impact of a 0.7 per unit grid voltage sag sustained for 50 milliseconds. The reactive and active grid powers, along with the instantaneous current and voltage of phase A, are depicted for all control methods and all three controllers return to steady-state operation within 400 ms of fault clearance.

5.4 Comparative Analysis and Control-Theoretic Interpretation

The performance differences observed in Table 6 and Figures 9-10 can be directly related to the fundamental nature of the control laws under consideration. The PI controller, designed via pole-zero cancellation methods, guarantees nominal tracking performance. Nevertheless, the linear nature of the PI controller is not effective in compensating the nonlinear relationship between the shoot-through duty cycle and the inductor current. As a result, the unmodeled dynamics introduced by the wind speed variation cause the observed ±13V voltage ripple on the v_{C1z} waveform. On the other hand, the robustness of the SMC is related to the existence of the sliding manifold that constrains the system trajectories over the operating points. As a result, the invariance property guarantees a reduction of over 60% in the voltage ripple compared to the PI controller. The unavoidable presence of the high-frequency chattering phenomenon, observed on the shoot-through control signal, is a fundamental trade-off related to the robust performance of the SMC. Nevertheless, the chattering phenomenon is observed to be within acceptable limits for the chosen switching frequency.

The FGS–PID controller is seen to have an intermediate position between the PI and the robust performance of the SMC. The gain scheduling employed in the FGS–PID controller guarantees a better performance in terms of the voltage ripple compared to the PI controller; the observed voltage ripple is reduced to ±10 V. Nevertheless, the performance is still dependent on the FGS control law and lacks the robustness guarantee of the invariance property. As a result, the FGS–PID controller is observed to have a slightly higher overshoot in the grid current waveform compared to the SMC during the grid voltage sag condition in Fig. 10.

From an applied point of view, the outcome of this comparison suggests that, for any given application where the minimum THD and maximal disturbance rejection are desired, SMC should be employed, regardless of the associated 'chattering' and increased complexity of implementation, since it offers the best possible outcome. If, instead, ease of implementation

[1] . field-programmable gate array

and existing PID-based infrastructure are of primary concern, then the FGS-PID method offers significant improvements over the fixed-gain PI method with only moderate additional complexity. Finally, the PI method should be considered for applications where conditions are benign and stability margins are high.

6 Practical Design and Stress Analysis

In order to determine the practical viability of the proposed qZSI in high-power applications, a comprehensive design and stress analysis of a 3-MW system will be presented in this section with the following working assumption:
- DC voltage input, □□□ = 1100V
- Reference capacitor voltage, □□1□□□ = 1400V
- Switching frequency, □□□ = 10.8 kHz
- qZSI inductance, □1 = □2 = □ = 25.8 μH
- qZSI capacitance, □1 = □2 = □ = 17.8 mF
- Modulation scheme: Simple Boost Control (SBC)
- The digital sampling frequency, □□ = 100 kHz

The work relies on existing steady-state, dynamic, and loss equations for impedance-source converters as described in [29].

6.1 Operating Point and Steady-State Stresses

The steady-state operating point is determined by the shoot-through duty cycle (D) and the boost factor (B).

6.1.1 Shoot-Through Duty Cycle and Boost Factor

From the qZSI voltage relationship:

$$V_{C1} = \frac{1-D}{1-2D} V_{in} \tag{57}$$

Solving for D with □□1 = 1400 V and □□□ = 1100 V:

$$1400 = \frac{1-D}{1-2D} \times 1100 \quad \Rightarrow \quad D \approx 0.1765 \tag{58}$$

The boost factor and the peak DC-link voltage across the inverter bridge are:

$$B = \frac{1}{1-2D} = \frac{1}{1-2\times 0.1765} \approx 1.545. \quad V_{PN} = B \cdot V_{in} = 1.545 \times 1100 \approx 1700\text{V} \tag{59}$$

6.1.2 Voltage Stresses

- Semiconductor devices (IGBTs and anti-parallel diodes) in the inverter bridge:
  Maximum voltage stress = $V_{PN} \approx 1700\text{V}$
- qZSI diode :
  Maximum reverse voltage = $V_{C1} + V_{C2} = V_{PN} \approx 1700\text{V}$ (during shoot-through)
- qZSI capacitors (C_1, C_2):
  $Rated\ DC\ voltage \geq (V_{C1} = 1400\text{V})$ and $\left(V_{C2} = \frac{D}{1-2D} V_{in} \approx 300\text{V}\right)$

6.1.3 Current Stresses

- Input and inductor average current: For an output power (P = 3 MW),

$$I_{in} = \frac{P}{V_{in}} = \frac{3\times 10^6}{1100} \approx 2727\text{A}. \quad I_{L1} = I_{L2} = I_{in} \tag{60}$$

- Inverter bridge average input current (I_{PN}): Estimated from power balance,

$$I_{PN.avg} \approx \frac{P}{V_{PN}} = \frac{3\times 10^6}{1700} \approx 1765\text{A} \tag{61}$$

- qZS diode average current: During shoot-through, the diode conducts the sum of the two inductor currents minus the inverter input current :

$$I_{D.avg} = 2I_L - I_{PN.avg} = 2 \times 2727 - 1765 \approx 3689\text{A} \tag{62}$$

The RMS current will be lower due to the duty cycle (D = 0.1765), but remains in the kiloampere range.

- qZS capacitor RMS current: Approximating the capacitor current waveform:

$$I_{C.rms} \approx \sqrt{D \cdot I_L^2 + (1-D)\cdot(I_{PN} - I_L)^2} \approx 1441\text{A}_{rms} \tag{63}$$

6.1.4 Ripple Calculations

- Inductor current ripple ((ΔI_L)): Using the volt-second balance during shoot-through (duration (DT_s), where ($T_s = 1/f_{sw} \approx 92.6\mu s$)):

$$\Delta I_L = \frac{(V_{in}+V_{C2})\cdot DT_s}{L} = \frac{(1100+300)\times 0.1765\times 92.6\times 10^{-6}}{25.8\times 10^{-6}} \approx 888\text{A}_{p-p} \tag{64}$$

The peak inductor current is ($I_{L.peak} = I_L + \Delta I_L/2 \approx 3171\text{A}$).

- Capacitor voltage ripple (ΔV_C):

$$\Delta V_C \approx \frac{I_{PN}\cdot DT_s}{C} = \frac{1765\times 0.1765\times 92.6\times 10^{-6}}{17.8\times 10^{-3}} \approx 1.62\text{ V} \tag{65}$$

6.2 Transient Behavior and Mitigation Strategies

Startup conditions must not damage the QZSI; therefore, several new methods have been implemented in series and improved qZSI topologies to provide additional protection for the qZSI.

- Through improvements in topology, the series qZSI/Improved qZSI has enabled controlling and/or eliminating low-impedance charging paths to charge the qZS capacitors by using different sites for the input diode. Therefore, the improved qZSI topologies will regulate current during operation by preventing the low-impedance charging path.
- Soft Start Controllers - The enhanced qZSI topologies use an improved digital control soft start sequence to control the startup sequence. The shoot through duty cycle increases at a predetermined rate to the rated/normal duty cycle during startup. Therefore, increasing the control voltage allows the qZS Capacitor(s) to stabilise at the proper voltage and prevents the qZSI from experiencing excessive current and/or over-voltage during Startup.
- Protective circuits - The control board and gate Driver are both designed with overcurrent and overvoltage protection. This protection is provided using Hall Effect sensors and voltage dividers.

6.3 Component Selection and Practical Implementation

To verify compatibility with commercially available components, the calculated stresses were compared with commercial semiconductor device specifications.

6.3.1 Semiconductor Devices

- The inverter bridge consists of press pack IGBT modules rated at 3300 V at 1200 A. The voltage rating of each module exceeds the 1.9-volt margin required for reliability (3300 V vs 1700 V). To meet the kA current requirement, each IGBT module position in the IGBT modules has three IGBT modules connected in parallel. Each IGBT module has its own gate driver and uses a symmetric busbar layout, enabling both static and dynamic current sharing.
- To accommodate the average current of 3700 A during shoot-through, four 3300 V, 1000 A fast recovery press pack diodes from the SSiC 3300 V series were connected together in a bank configuration to form one diode.

6.3.2 Passive Components

- qZS Inductors ($L = 25.8\mu$H): Custom-designed, liquid-cooled inductors are required. The core will use amorphous metal (e.g., Metglas) for its low core loss at 10.8 kHz and high saturation flux density. The windings will be made from hollow copper conductors, enabling direct water cooling to reduce copper losses. Mechanical bracing is included to withstand Lorentz forces at peak current ($\sim 3.2KA$).
- qZS Capacitors ($C = 17.8$mF): This is realized as a parallel array of high-ripple-current, DC-link film capacitor modules (e.g., TDK B25620 series, 2 mF, 1500V). Nine such units per capacitor branch provide the required capacitance and voltage rating while distributing the 1441 Amps. Low-inductance busbar connections are critical.

6.3.3 Control Hardware

A Texas Instruments TMS320F28379D dual-core DSP (or equivalent) is specified. Its 200 MHz clock rate easily supports the 100 KHz sampling frequency (f_s), enabling the cascade-loop control, SBC modulation, and protection routines to execute within $10\mu s$.

6.4 Justification of Switching and Sampling Frequencies

- Switching Frequency ($f_{sw} = 10$kHz): 10.8 kHz is a design decision that balances increased frequency with the more classic range of 1 to 3 kHz. This decision was made to reduce the physical size of the passive components in the qZS design, since inductance and capacitance are inversely proportional to the switching frequency. As such, reducing passive component size was imperative in applications with strict size and weight limits, especially in offshore wind turbine nacelles and propulsion systems. The increase in switching losses associated with this decision is countered by the new advanced liquid-cooling system previously discussed.
- Sampling Frequency ($f_s = 100$kHz): This provides over 9 samples per switching cycle, which is sufficient to implement accurate double-loop control, space vector modulation, and rapid fault protection. It is well within the capability of modern DSPs and ensures control bandwidth high enough to manage the dynamics of the qZS network and the grid interface.

6.5 Conclusion on Practical Feasibility

Using current power electronics technologies, this report presents a thorough analysis of all stresses and components that prove a 3 MW qZSI can operate at all specified conditions. The stresses on the voltages and currents will be high; however, these stresses will remain within the specifications of the 3300 V class press-pack IGBT, diode, and specially manufactured passive components available on the market today. This report will also address the three main obstacles, including managing kiloampere currents, generating a high-frequency ripple in the magnetics, and managing thermal dissipation. All three of these challenges have been resolved by applying high-power engineering techniques, such as paralleling devices, designing magnets specifically for this application, and using forced liquid cooling to prevent device overheating. This report shows how a qZSI system can balance high power density (achieved through higher switch frequencies) with high power efficiency, making this type of system a viable option for future compact renewable energy and drive systems.

7 Conclusion

A GAM model of the qZSI, has been employed. This model enabled the implementation and assessment of three different control strategies for a wind turbine-based PMSG utilizing vector control. The performance of the PI controller, SMC, and FGS-PID was assessed under identical operational conditions, revealing significant differences in their capabilities. All three control mechanisms were tested in standard grid scenarios, providing valuable insights into their operational effectiveness. The following quantitative findings are established:

Capacitor voltage ripple:

- PI: ±13V, 0.92%
- FGS-PID: ±10V, 0.71%
- SMC: ±5V, 0.35%

The SMC controller reduces voltage ripple by a significant 62% compared to the PI controller.

Grid current THD:

- PI: ≤3%
- FGS-PID: ≤2.5%
- SMC: ≤1.8%

The SMC controller reduces THD by a significant 40% compared to the PI controller.

Transient response (grid fault recovery):

- PI overshoot: 41.1%
- FGS-PID overshoot: 36.2%
- SMC overshoot: 31.7%

While the PI controller performs well under stable conditions, it struggles to handle wind speed fluctuations, leading to notable voltage fluctuations in the capacitor. During transient recovery following a grid fault, the grid current measured for the PI and FGS-PID controllers is slightly higher than that of the SMC controller. An HIL setup was developed to validate the performance of the three controllers under diverse operating conditions, confirming their satisfactory operation.

In contrast, the SMC demonstrates smooth operation under varying wind speeds, consistently outperforming the other controllers. It exhibits superior performance in terms of stability and transient response. Although the FGS-PID is perceived as a straightforward controller, it has limitations and requires significant computational resources. In conclusion, the SMC emerges as a highly effective and reliable control strategy for wind turbine-based PMSG systems, offering robust performance under dynamic conditions.

8 References

[1] I. Toumi, A. Boulmaiz, B. Meghni, and O. Hachana, "Robust variable step P&O algorithm based MPPT for PMSG wind generation system using estimated wind speed compensation technique," *Sustainable Energy Technologies and Assessments*, vol. 60, p. 103420, 2023.

[2] E. Muñoz-Palomeque, J. E. Sierra-García, and M. Santos, "Wind turbine maximum power point tracking control based on unsupervised neural networks," *Journal of Computational Design and Engineering*, vol. 10, no. 1, pp. 108-121, 2023.

[3] A. Bakbak, H. T. Canseven, M. Ayaz, M. Altintaş, and E. Meşe, "Maximizing energy extraction from direct grid coupled PMSG for wind energy conversion systems," *IEEE Transactions on Industry Applications*, vol. 58, no. 3, pp. 3888-3900, 2022.

[4] X. Lyu and D. Groß, "Grid forming fast frequency response for PMSG-based wind turbines," *IEEE Transactions on Sustainable Energy*, vol. 15, no. 1, pp. 23-38, 2023.

[5] M.-K. Nguyen and T.-T. Tran, "A single-phase single-stage switched-boost inverter with four switches," *IEEE Transactions on Power Electronics*, vol. 33, no. 8, pp. 6769-6781, 2017.

[6] J. Anderson and F. Z. Peng, "Four quasi-Z-source inverters," in *2008 IEEE Power Electronics Specialists Conference*, 2008: IEEE, pp. 2743-2749.

[7] M.-K. Nguyen, Y.-C. Lim, and G.-B. Cho, "Switched-inductor quasi-Z-source inverter," *IEEE Transactions on Power Electronics*, vol. 26, no. 11, pp. 3183-3191, 2011.

[8] Y. Zhang, Y. Liu, B. Luo, and Y. Ling, "Variable weight coefficient MPC control strategy for qZSI-VSG wind power grid-connected system," *IET renewable power generation*, vol. 17, no. 8, pp. 1952-1965, 2023.

[9] E. P. Soares-Ramos, L. De Oliveira-Assis, R. Sarrias-Mena, P. García-Triviño, C. A. García-Vázquez, and L. M. Fernandez-Ramirez, "Averaged dynamic modeling and control of a quasi-Z-source inverter for wind power applications," *IEEE Access*, vol. 9, pp. 114348-114358, 2021.

[10] A. Athwer and A. Darwish, "A review on modular converter topologies based on WBG semiconductor devices in wind energy conversion systems," *Energies*, vol. 16, no. 14, p. 5324, 2023.

[11] L. Monjo, L. Sainz, J. J. Mesas, and J. Pedra, "Quasi-Z-source inverter-based photovoltaic power system modeling for grid stability studies," *Energies*, vol. 14, no. 2, p. 508, 2021.

[12] B. Ge *et al.*, "Current ripple damping control to minimize impedance network for single-phase quasi-Z source inverter system," *IEEE Transactions on Industrial Informatics*, vol. 12, no. 3, pp. 1043-1054, 2016.

[13] Y. Li, S. Jiang, J. G. Cintron-Rivera, and F. Z. Peng, "Modeling and control of quasi-Z-source inverter for distributed generation applications," *IEEE Transactions on Industrial Electronics*, vol. 60, no. 4, pp. 1532-1541, 2012.

[14] L. Monjo and L. Sainz, "State-space model of qZSI based PMSG-WPGSs for transient dynamic studies," in *2021 IEEE International Conference on Environment and Electrical Engineering and 2021 IEEE Industrial and Commercial Power Systems Europe (EEEIC/I&CPS Europe)*, 2021: IEEE, pp. 1-5.

[15] M. Diaz-Bustos, C. R. Baier, M. A. Torres, P. E. Melin, and P. Acuna, "Application of a control scheme based on predictive and linear strategy for improved transient state and steady-state performance in a single-phase quasi-Z-source inverter," *Sensors*, vol. 22, no. 7, p. 2458, 2022.

[16] S. Vadi and R. Bayindir, "Modeling, analysis and proportional resonant and proportional

integral based control strategy for single phase quasi-Z source inverters," *IEEE Access,* vol. 10, pp. 87217-87226, 2022.
[17] P. Janavi, P. Manoharan, and P. Deepamangai, "Control Strategy for Switched-Impedance Quasi-Z-Source Inverter," in *2022 Second International Conference on Advances in Electrical, Computing, Communication and Sustainable Technologies (ICAECT)*, 2022: IEEE, pp. 1-5.
[18] A. Zakipour, S. Shokri Kojori, and M. Tavakoli Bina, "Closed-loop control of the grid-connected Z-source inverter using hyper-plane MIMO sliding mode," *IET Power Electronics,* vol. 10, no. 15, pp. 2229-2241, 2017.
[19] K. H. Law and W. P. Q. Ng, "Dual Closed-Loop Scheme with Lead Compensator and Proportional Controller for Quasi Z-Source Inverter Based STATCOM," in *2018 IEEE 7th International Conference on Power and Energy (PECon)*, 2018: IEEE, pp. 56-61.
[20] B. Xu and X. Ran, "Sliding mode control for three-phase quasi-Z-source inverter," *IEEE Access,* vol. 6, pp. 60318-60328, 2018.
[21] M. M. Bajestan, H. Madadi, and M. A. Shamsinejad, "Control of a new stand-alone wind turbine-based variable speed permanent magnet synchronous generator using quasi-Z-source inverter," *Electric Power Systems Research,* vol. 177, p. 106010, 2019.
[22] M. Bubalo, M. Bašić, D. Vukadinović, and I. Grgić, "Optimized isolated operation of a WECS-powered microgrid with a battery-assisted qZSI," in *2020 6th International Conference on Electric Power and Energy Conversion Systems (EPECS)*, 2020: IEEE, pp. 1-6.
[23] S. Bayhan, M. Trabelsi, H. Abu-Rub, and M. Malinowski, "Finite-control-set model-predictive control for a quasi-Z-source four-leg inverter under unbalanced load condition," *IEEE Transactions on Industrial Electronics,* vol. 64, no. 4, pp. 2560-2569, 2016.
[24] A. Ayad, P. Karamanakos, and R. Kennel, "Direct model predictive current control strategy of quasi-Z-source inverters," *IEEE Transactions on Power Electronics,* vol. 32, no. 7, pp. 5786-5801, 2016.
[25] V. Yaramasu and B. Wu, *Model predictive control of wind energy conversion systems*. John Wiley & Sons, 2016.
[26] V. Yaramasu, "Predictive control of multilevel converters for megawatt wind energy conversion systems," *Ryerson University,* 2014.
[27] A. Uehara *et al.*, "A coordinated control method to smooth wind power fluctuations of a PMSG-based WECS," *IEEE Transactions on energy conversion,* vol. 26, no. 2, pp. 550-558, 2011.
[28] K. Mokhtari, S. Shokri-Kojori, and M. Aliyari-Shoorehdeli, "A new generalized state-space averaged model, control design and stability analysis for three phase grid-connected quasi-Z-Source inverters," *International Journal of Electrical Power & Energy Systems,* vol. 158, p. 109932, 2024.
[29] Y. Liu, H. Abu-Rub, B. Ge, F. Blaabjerg, O. Ellabban, and P. C. Loh, *Impedance source power electronic converters*. John Wiley & Sons, 2016.
[30] F. Bagheri, H. Komurcugil, O. Kukrer, N. Guler, and S. Bayhan, "Multi-input multi-output-based sliding-mode controller for single-phase quasi-Z-source inverters," *IEEE Transactions on Industrial Electronics,* vol. 67, no. 8, pp. 6439-6449, 2019.
[31] A. Bakeer, M. A. Ismeil, and M. Orabi, "A powerful finite control set-model predictive control algorithm for quasi Z-source inverter," *IEEE Transactions on Industrial Informatics,* vol. 12, no. 4, pp. 1371-1379, 2016.
[32] X. Duan, L. Kang, H. Zhou, and Q. Liu, "Multivector model predictive power control with low computational burden for grid-tied quasi-Z-source inverter without weighting factors," *IEEE Transactions on Power Electronics,* vol. 37, no. 10, pp. 11739-11748, 2022.
[33] M. Mosa, R. S. Balog, and H. Abu-Rub, "High-performance predictive control of quasi-impedance source inverter," *IEEE Transactions on Power Electronics,* vol. 32, no. 4, pp. 3251-3262, 2016.
[34] Y. Liu, B. Ge, H. Abu-Rub, H. Sun, F. Z. Peng, and Y. Xue, "Model predictive direct power control for active power decoupled single-phase quasi-Z-source inverter," *IEEE Transactions on Industrial Informatics,* vol. 12, no. 4, pp. 1550-1559, 2016.
[35] W. Liang, Y. Liu, B. Ge, H. Abu-Rub, R. S. Balog, and Y. Xue, "Double-line-frequency ripple model, analysis, and impedance design for energy-stored single-phase quasi-Z-source photovoltaic system," *IEEE Transactions on Industrial Electronics,* vol. 65, no. 4, pp. 3198-3209, 2017.
[36] Z. Rasin, M. F. Rahman, M. Azri, M. H. N. Talib, and A. Jidin, "Design and development of grid-connected quasi-z-source pv inverter," *International Journal of Power Electronics and*

Drive Systems (IJPEDS), vol. 9, no. 4, pp. 1989-2005, 2018.

Biographies

Kazem Mokhtari received the Master's degree in the Electrical Engineering in 2018 from Noshirvani University Iran. Currently, He is doing Ph.D. from the Department of Electrical Engineering at KNTU, Iran. He has published some papers in various reputed journals. His research areas are Renewable energy system integration, Smart Grid and control.

Shokrolah Shokri Kojori received his B.Sc. and M.Sc. degrees from Tabriz University, Tabriz, Iran, in 1975 and 1977, respectively. He then obtained his Ph.D. degree from Bath University, U.K., in 1988. He is currently an Associate Professor of the Department of Electrical Engineering, at KNTU. His current research interests include electrical machine analysis, modeling of electric machines and transformers, and power systems dynamic and control.

Mahdi Aliyari Shoorehdeli received his B.Sc. degree in electronics engineering from KNTU in 2001. He then pursued his studies in control engineering and, therefore, obtained his M.Eng. and Ph.D. degree from the same university in 2003 and 2008, respectively. He is currently appointed to the Department of Mechatronics Engineering of KNTU as an Assistant Professor. Dr. Aliyari is the author of more than 100 papers in international journals and conferences. His research interests include fault detection and isolation and system identification and optimization.